Electro-Thermal Stress Analysis and Lifetime Evaluation of DC-Link Capacitor banks in the Railway Traction Drive System

Yao, Bo; Ge, Xinglai; Xie, Dong; Li, Songtao; Zhang, Yichi; Wang, Huimin; Wang, Haoran

Published in:
IEEE Journal of Emerging and Selected Topics in Power Electronics

DOI (link to publication from Publisher):
10.1109/JESTPE.2020.3000130

Publication date:
2020

Document Version
Accepted author manuscript, peer reviewed version

Electro-Thermal Stress Analysis and Lifetime Evaluation of DC-Link Capacitor banks in the Railway Traction Drive System

Bo Yao, *Student Member, IEEE*, Xinglai Ge, *Member, IEEE*, Dong Xie, *Student Member, IEEE*, Songtao Li, Yichi Zhang, Huimin Wang, *Student Member, IEEE*, and Haoran Wang, *Member, IEEE*

***Abstract*- In the railway traction drive system, the reliability of DC-link capacitor banks faces enormous challenges due to the multi-operation conditions, the complex physical structures, and the safe operation requirements. Considering these issues, this paper proposes a reliability evaluation method of the DC-link capacitors banks to provide a guideline for preventive maintenance in the traction drive system. In the electro-thermal stress analysis, different from the conventional methods, the dynamic power loss profile is obtained by the sliding-window discrete Fourier transform (DFT) and the equivalent series resistance is fitted by the neural network. Afterward, a bidirectional thermal model is established to estimate the thermal stress under the dynamic power losses, considering the impact of thermal capacity, thermal coupling, and air-cooling heat dissipation. In addition, according to stability analysis and the rated temperature limitation, an end-of-lifetime standard that meets the safe operation requirement of the train is firstly proposed, thereby evaluating the lifetime bottleneck of the DC-link capacitor banks. The evaluation results can provide a reference to use the lower-cost on-condition maintenance instead of scheduled maintenance in the railway traction drive system. Furthermore, a prototype experiment is performed to verify the effectiveness of the electro-thermal stress model.**

***Index Terms*-- DC-link capacitor, multi-operation conditions, railway traction drive system, electro-thermal stress, lifetime**

I. INTRODUCTION

In the railway traction system, due to strict safety requirements, passive components usually require the high lifetime of more than decades [1]. In recent years, studies of the reliability evaluation mainly focus on the analysis of fault data statistics in the railway traction system, including the establishment of databases, the modeling of reliability index, the fuzzy synthetic evaluation, and the analysis of fault tree [2]-[5]. However, because the sample size of the fault data is uncertain, the existing methods have certain randomness and limitation, and rarely involve the reliability evaluation of capacitor in the traction system. In the railway traction drive system, the DC-link capacitor, as the role of realizing energy storage and filtering, is located between the rectifier and the inverter [6]. More importantly, it is highly related to the system safety and reliability. Therefore, the reliability evaluation of the DC-link capacitor banks is essential for the operation and maintenance in railway traction system [7].

In recent years, some reliability evaluation methods for DC-link capacitors have been proposed. The lifetime mathematical model of the DC-link capacitor is given and the failure criterion is analyzed in [8]. Based on the failure criterion, the calculation method of the capacitance loss is shown to analyze the capacitor aging trend [9]-[10]. Furthermore, the capacitor lifetime estimation method considering the influence of the nonlinear cumulative damage is accomplished in [11]. Recently, the film capacitor has been gradually applied because of the potential reliability improvement and cost reduction [12]. According to the variation of the capacitor parameters, the lifetime model of the film capacitor with the Poisson distribution is presented in [13]-[14]. However, the actual end-of-life standards of the DC-link capacitor in application systems is neglected in most of existing methods. Due to the stringent safety requirements in the railway traction drive system, the lifetime bottleneck of the DC-link capacitor that meets the safe operation needs to be studied.

The mission profiles cannot be ignored in the reliability evaluation of the DC-link capacitor [15]. The influence of wind speed and ambient temperature on the lifetime of the DC-link capacitor in the wind power system are analyzed in [16]-[17]. An instantaneous electro-thermal method is discussed to analyze the mission profiles in the photovoltaic system in [18]. Furthermore, the impact of the photovoltaic array size on the capacitor reliability is analyzed in [19]. Meanwhile, the solar irradiance at small timescales is handled by the instantaneous electro-thermal method [20]. However, according to the multi-operation conditions in the railway, the complex mission profiles need to be dealt with, including the short-term changes in speed and slope as well as the long-term changes in ambient temperature and humidity [21]-[22]. Therefore, the electro-thermal stress analysis with the dynamic power losses should be resolved well.

In the reliability analysis, the thermal stress of the capacitor is a key factor that wears down and reduces the lifetime [8]. Most of existing works mainly use the independent mathematical models to address the issue of the thermal stress of capacitor [11], [14], and [16]-[20], but the influence of the thermal capacity, thermal coupling, and potential air cooling are ignored. The material, geometric, and thermal properties of capacitor can be simulated in the multi-physics model [23]-[24].

This work was supported by the Project Supported by High-Speed Railway Joint Funds of the National Natural Science Foundation of China (U1934204) and the Project Supported by National Natural Science Foundation of China (51677156, 61733015). (*Corresponding author: Xinglai Ge*).

B. Yao, X. Ge, D. Xie, S. Li, Y. Zhang, and H. Wang are with the Ministry of Education Key Laboratory of Magnetic Suspension Technology and Maglev Vehicle, Southwest Jiaotong University, Chengdu 610031, China (e-mail: yaobo1666@my.swjtu.edu.cn; xlgee@163.com; xiedong@my.swjtu.edu.cn; SongtaoLi@my.swjtu.edu.cn; yichizhang@my.swjtu.edu.cn; wanghuimin@my.swjtu.edu.cn).

H. Wang is with the Department of Energy Technology, Aalborg University, Aalborg 9220, Denmark (e-mail: hao@et.aau.dk).

This article has been accepted for publication in a future issue of this journal, but has not been fully edited. Content may change prior to final publication. Citation information: DOI 10.1109/JESTPE.2020.3000130, IEEE Journal of Emerging and Selected Topics in Power Electronics

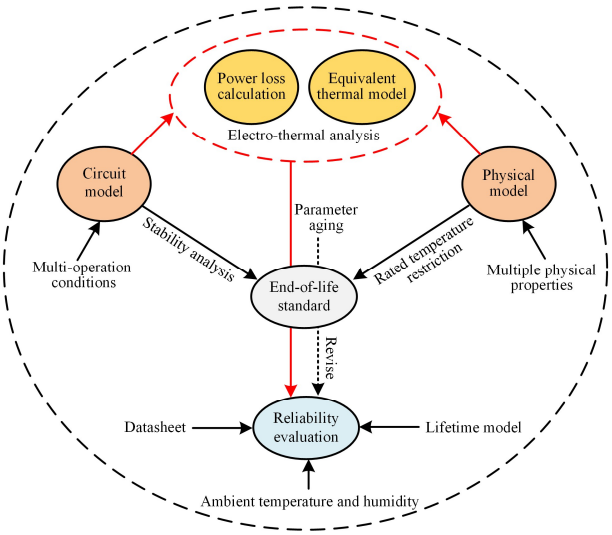

Fig. 1. Reliability evaluation scheme of DC-link capacitor banks.

However, the requirement of large capacitance and high voltage in the railway traction drive system leads to complex physical structure, where the multiple series-parallel capacitor banks need to be further discussed. An equivalent thermal model is established to analyze the thermal distribution of capacitor banks, which takes into account the thermal coupling between the capacitors [25]. Furthermore, the equivalent thermal model is simplified by the RC circuit network in [26], but the effect of electro-thermal coupling stress is not considered. Therefore, it is necessary to establish an equivalent thermal model according to the actual physical structure and consider the effects of dynamic power losses on the electro-thermal analysis.

In this paper, a reliability evaluation method of the DC-link capacitor banks is proposed for the railway traction drive system. The evaluation scheme is shown in Fig. 1. Firstly, the circuit model and the physical model are established by multi-operation conditions and multiple physical properties. In the electro-thermal analysis, the dynamic power loss profile is obtained by using the sliding-window discrete Fourier transform (DFT) and the equivalent series resistance (ESR) is fitted by the neural network. Furthermore, the bidirectional equivalent thermal model based on the electro-thermal coupling is presented according to the multiple physical properties and dynamic power losses. Meanwhile, as the film capacitor degrades, the capacitor parameters are affected by the stability criterion and the rated temperature limitation. Finally, the end-of-lifetime standard that meets the safe operation requirement is proposed, thereby evaluating the lifetime bottleneck of the DC-link capacitor banks in the railway traction drive system.

This rest of this paper is structured as follows: Section II analyzes the electrical model and the multiple physical property models of the DC-link capacitor. In Section III, the electro-thermal stress of the capacitor banks is analyzed by the dynamic power loss profile and the bidirectional thermal model. In Section IV, the electrical and thermal stress analysis is verified by a prototype experimental platform. Section V obtains the end-of-life standard and lifetime bottleneck of DC-link capacitor banks that meet the safe operation.

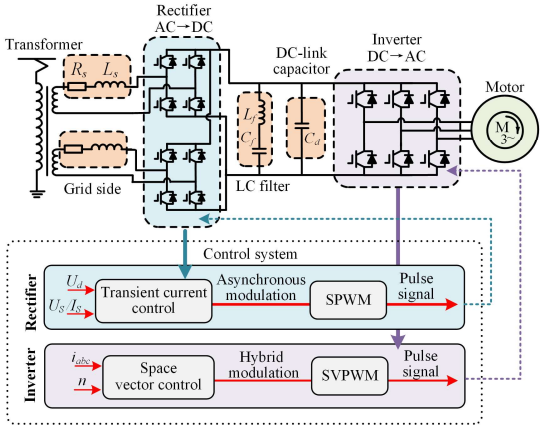

Fig. 2. Typical circuit model of railway traction drive system.

TABLE I
PARAMETERS OF THE TRACTION MOTOR DRIVES AND CAPACITOR BANKS

Traction drive system parameters	
Grid side voltage/frequency	U_s=1550 V/50 Hz
Grid side equivalent resistance /inductance	R_s =0.2 Ω/ L_s=2.3 mH
Switching frequency	450 Hz (rectifier) / 1000 Hz (inverter)
Rate DC-Link voltage	U_r=3600 V
Filter inductor/capacitor	L_f=0.83 mH / C_f=3 mF
Motor rated power / frequency	P_0=562 kV•A / 138 Hz
DC-link Capacitor banks parameters (Four parallel)	
Rated capacitance	C_d=3000 μF (750 uF×4)
Rated voltage	U_0=4000 V
Equivalent series resistance	ESR =0.45 mΩ (10 KHz/20°C)
Thermal resistance	R_{th}=0.72 K/W
Rate load lifetime	L_0=100000 h (4000 V/70°C)
Dielectric dissipation factor	$\tan\delta_0=2\times10^{-4}$
Hot pot temperature range	-50~75°C

II. ELECTRICAL AND PHYSICAL MODEL

A. *Electrical Model of the Traction Drive System*

A typical railway traction drive system is shown in Fig. 2 [27]-[28]. The rectifier module adopts the transient current control algorithm with the SPWM, where the equivalent switching frequency of the rectifiers is doubled by the multiplexing method [29]. The field-oriented control with the SVPWM are used for the inverter. The DC-link capacitor is located in the middle of the two rectifiers and the traction inverter. The main parameters of the traction drive system and DC-link capacitor are given in Table I.

In the railway traction drive system, the multi-operation conditions mainly include the running speed profile and the running slope profile, which are given in Fig. 3. Through the drag calculation, the running speed v and slope s are converted into speed drag $F(datum)$ and slope drag $F(slope)$, respectively. The $F(total)$ represents the total drag [21]

$$\begin{cases} F_{(slope)} = m_{stat} g \times s / 1000 \\ F_{(datum)} = m_{stat} g \times (7.75 + 0.062367v + 0.00113v^2) \\ F_{(total)} = F_{(slope)} + F_{(datum)} \end{cases} \quad (1)$$

This article has been accepted for publication in a future issue of this journal, but has not been fully edited. Content may change prior to final publication. Citation information: DOI 10.1109/JESTPE.2020.3000130, IEEE Journal of Emerging and Selected Topics in Power Electronics

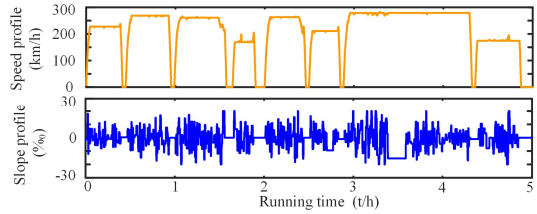

Fig. 3. Mission profile waveform of running speed and slope.

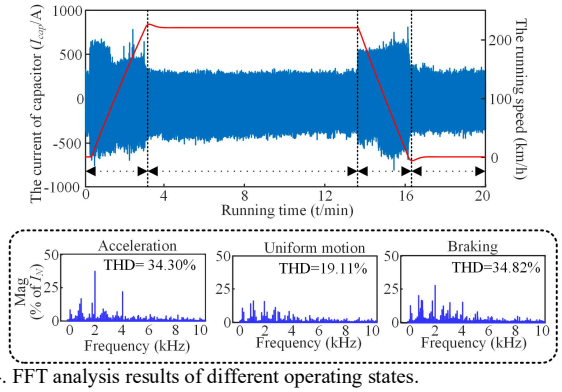

Fig. 4. FFT analysis results of different operating states.

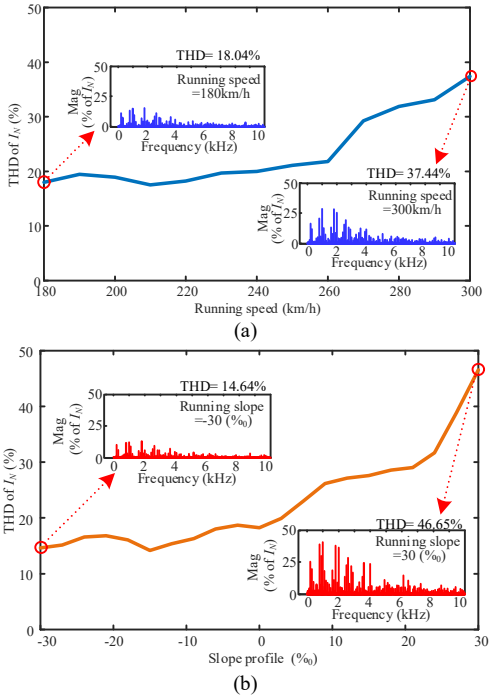

Fig. 5. FFT analysis results. (a) Different running speed (running slope=0‰). (b) Different running slope (running speed=220km/h).

where m_{stat} and g represent the dynamic mass of trains and the acceleration of gravity, respectively.

The motor speed n is proportional to the running speed v, which can be expressed as [22]

$$n = \frac{60a \times v}{3.6 \times \pi \times d} \tag{2}$$

Meanwhile, the motor load torque T_L is proportional to the total drag $F(total)$, which can be expressed as

$$T_L = \frac{F_{(total)} \times d}{2 \times N \times a \times \eta_c} \tag{3}$$

where d, a, n_p, N and η_c denote the wheel diameter, the pole pairs of the motor, the gear ratio, the total number of motors, and the gear transmission efficiency, respectively.

Considering the torque balance requirement of asynchronous motor, the electromagnetic torque T_e is given by

$$T_e = T_L + \frac{J}{n_p}\frac{dn}{dt} \tag{4}$$

where J is the moment of inertia.

According to MT rotating coordinate system in the vector control, T_e can be expressed as

$$T_e = n_P L_m \left(i_{sT} i_{rM} - i_{sM} i_{rT}\right) = n_p \frac{L_m}{L_r}\left(i_{sT}\psi_{rM} - i_{sM}\psi_{rT}\right) \tag{5}$$

where L_r, L_m, i_{sT}, i_{rT}, i_{sM}, i_{rM}, Ψ_{rT}, and Ψ_{rM} denote the rotor self-inductance, the mutual inductance between stator and rotor, the stator current in T-axis, the rotor current in T-axis, the stator current in M-axis, the rotor current in M-axis, the rotor flux linkage in T-axis, and the rotor flux linkage in M-axis, respectively.

Under the condition satisfying the rotor flux orientation, it can be obtained [30]

$$\psi_{rT} = 0,\ i_{rM} = 0 \tag{6}$$

Substituting (6) into (5), it can be obtained that i_{sT} is positively related to T_e

$$i_{sT} = \frac{T_e L_r}{n_P L_m \psi_{rM}} \tag{7}$$

Subsequently, the motor stator currents i_A, i_B, and i_C can be obtained by *Park* inverse transformation ($C_{2/3}$)

$$\begin{bmatrix} i_{sT} & i_{sM} \end{bmatrix}^T \Rightarrow C_{2/3} \Rightarrow \begin{bmatrix} i_A & i_B & i_C \end{bmatrix}^T \tag{8}$$

The root mean square (RMS) value of the DC-link capacitor current I_{rms} can be expressed by [31]

$$I_{rms} = I_N \sqrt{\frac{M}{2\pi}\left[4\sqrt{3}\left(4\cos 2\Phi + 6\right) - 9\pi M\left(\cos 2\Phi + 1\right)\right]} \tag{9}$$

where M, I_N, and Φ are the modulation index, the current amplitude of three-phase stator current i_A, i_B, and i_C, and the phase delay of the i_A, i_B, and i_C with respect to the fundamental voltage, respectively.

It can be given from the above mathematical model that T_e is approximately equal to T_L (dn/dt = 0) when the traction drive system operates under uniform motion state. Since T_e, i_{sT}, i_{ABC}, and I_N vary with the running slope and speed, I_{rms} also changes dynamically. I_{rms} increases with the higher slope and the faster speed. When the traction drive system operates under the acceleration and braking states, the absolute value of T_e increases with the increase of the train acceleration (dn/dt), where the values of I_{rms} are larger than that under the uniform motion state.

The total harmonic distortion (THD) is obtained from the harmonic spectrum of the capacitor current, as shown in Fig. 4 and 5. It can be seen that the THD values of the capacitor current in the acceleration and braking stages are much higher

This article has been accepted for publication in a future issue of this journal, but has not been fully edited. Content may change prior to final publication. Citation information: DOI 10.1109/JESTPE.2020.3000130, IEEE Journal of Emerging and Selected Topics in Power Electronics

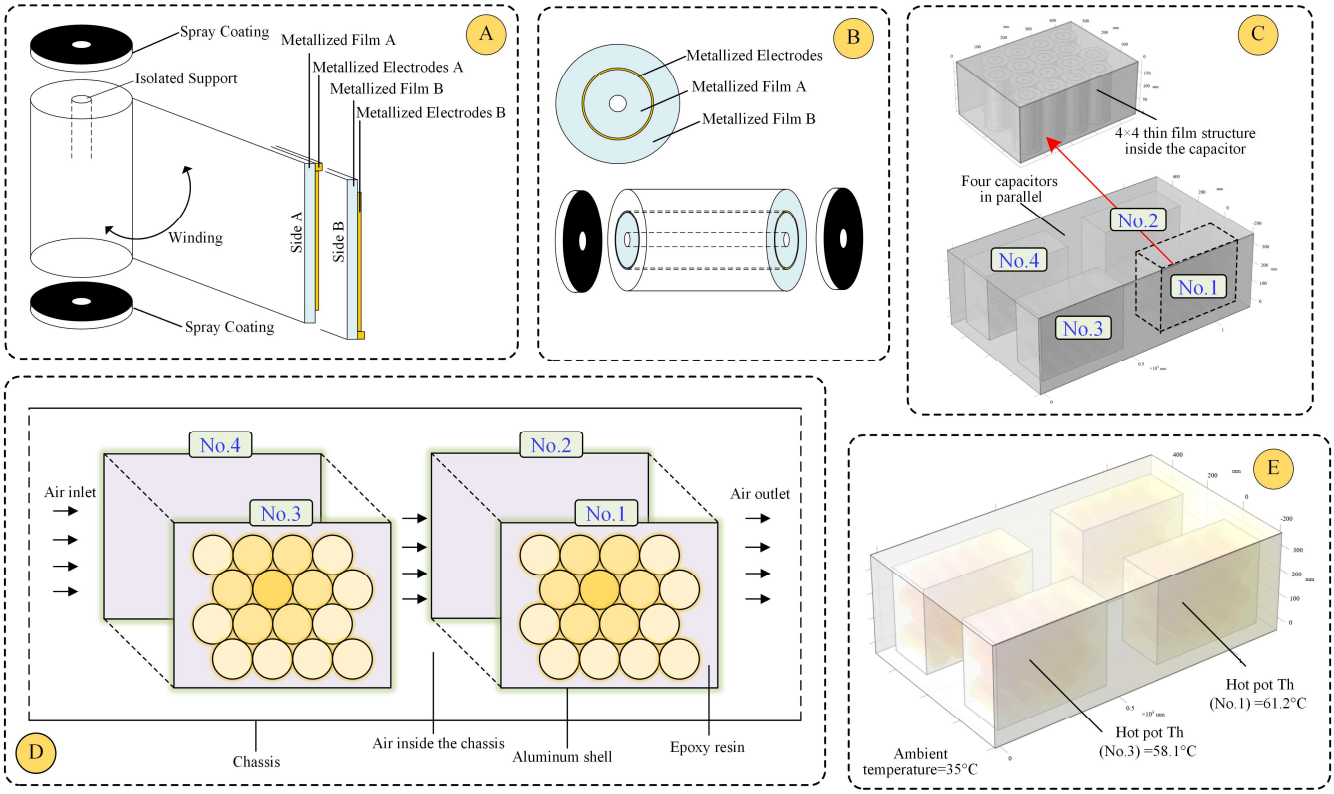

Fig. 6. Multiple physical properties modeling of DC-link capacitor banks.

than that of the uniform motion state. As the running speed increases, the THD value of I_{rms} gradually increases. The THD value at 300 km/h is about twice as much as that at 180 km/h. Meanwhile, as the running slope increases, the THD value of I_{rms} increases rapidly. When the running slope is 30‰, the THD value reaches 46.65%. The result shows that the speeds and slopes have the significant impacts on the electrical stress of the DC-link capacitor. It means the effect of the operating states, speed and slope on the electrical stress of the capacitor should be considered.

B. Multiple Physical Properties Modeling

In order to analyze the thermal stress, according to the geometric dimensions, physical parameters and material properties of the actual capacitor banks, the multiple physical properties model is established by the finite element simulation, as shown in Fig. 6 [23] [24].

The DC-link capacitors used in the railway traction drive system are composed of serval polypropylene film units. As given in Fig. 6(A), in each polypropylene film unit, two film layers are wound around a cylindrical mandrel. After winding, each side is sprayed with zinc metal particles. The thin metal electrode (the metallized electrodes A and metallized electrodes B) evaporated onto the film is of the order of nanometers. The thickness of the polypropylene dielectric (the metallized film A and metallized film B) is of the order of microns.

Considering the difficulty of the physical modeling with the winding structure, it is necessary to establish an equivalent physical structure. Since the metallized electrode is covered by the metallized film during the winding process, according to the actual overall thickness in the equivalent model, the metallized electrodes in a film structure are equivalent to the single layer in the cylinder as shown in Fig. 6(B). In addition, the metallized electrodes in the middle ring structure is respectively wrapped by equivalent metallized film A and metallized film B.

In Fig. 6(C), the material properties (including thermal conductivity, heat capacity, and density) and the thermal properties (including heat flux and heat dissipation) are considered in the physical modeling. Meanwhile, according to the medium refractive index of different materials, the radiative heat transfer boundaries are set on the surface of the capacitor.

The overall distribution of the internal and external structures of the capacitor is shown in Fig. 6(D), where each capacitor is closely packed by 16 separate film structures and filled with the insulating epoxy. Besides, by setting the cooling coefficient and the cooling channel, the influence of the air-cooled heat dissipation on the capacitor is analyzed.

The heat sources are set in the metallized electrodes of each film core, and the ambient temperature outside the capacitor banks is considered. The thermal stress of the capacitor banks is obtained by finite element meshing, as shown in Fig. 6(E). Furthermore, the temperature distribution of each layer is obtained by setting different heat sources.

III. Electro-thermal Coupling Analysis

A. Power Loss Calculation of DC-link Capacitor

This article has been accepted for publication in a future issue of this journal, but has not been fully edited. Content may change prior to final publication. Citation information: DOI 10.1109/JESTPE.2020.3000130, IEEE Journal of Emerging and Selected Topics in Power Electronics

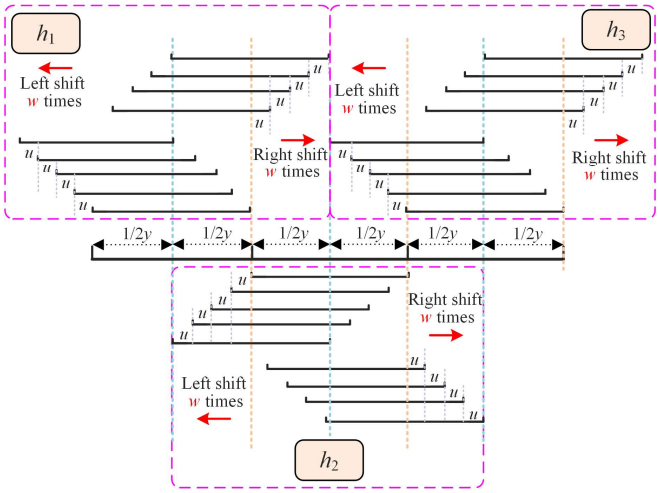

Fig. 7. Sliding-window method in DFT.

The heat of the capacitor is mainly generated by the power loss, which is closely related to the ESR, the current and frequency of the DC-link capacitor [8]. The power loss can be expressed as [11]

$$P_{loss}=\sum_{i=1}^{n}\left[ESR(f_i)\times I_{rms}^{2}(f_i)\right] \tag{10}$$

where $ESR(f_i)$ and $I_{rms}(f_i)$ represent the ESR and the RMS value of the ripple current at frequency f_i, respectively.

To characterize the dynamic change of electrical stress, the discrete values of I_{rms} are grouped into $\{h_1,h_2,h_3,\ldots,h_k\}$. The DFT of the discrete signal $I_{rms}(h_k)$ in the kth group is

$$I_{rms}(h_k,f_i)=S_{DFT}(I_{rms}(h_k)) \tag{11}$$

where $I_{rms}(h_k,f_i)$ represents the harmonic amplitude of I_{rms} when the frequency is f_i. in the kth group. Meanwhile, f_i is taken from 20 to 10kHz (take at interval 1) [32].

The sliding-window method is used in the group $\{h_1,h_2,h_3,\ldots,h_k\}$. The each grouping module is shifted left by w units as $\{(h_k,-1), (h_k,-2), (h_k,-3),\ldots, (h_k,-w)\}$ and shifted right by w units as $\{(h_k,1), (h_k,2), (h_k,3),\ldots, (h_k,w)\}$, totaling $2w+1$ units to calculate the average value $I_{rms}^{*}(h_k,f_i)$

$$I_{rms}^{*}(h_k,f_i)=\frac{\sum_{m=-w}^{w}\left[S_{DFT}(I_{rms}(h_k,\ m))\right]}{2w+1} \tag{12}$$

As shown in Fig. 7, the sliding-window grouping fully covers the I_{rms} to reflect the dynamic change of the capacitor current, thereby reducing the error of artificial grouping. The relationship between grouping and sliding-window length should satisfy

$$\frac{1}{2}y=u\times w \tag{13}$$

where u and y represent the sliding-window moving distance and the sliding-window length, respectively.

Thus, the DFT analysis of I_{rms} with sliding-window grouping can be expressed as

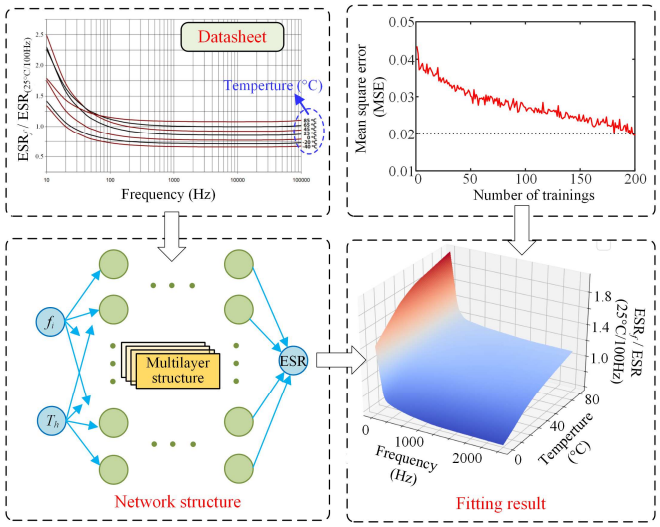

Fig. 8. Neural network fitting of the ESR.

$$I_{rms}(f_i)=\begin{bmatrix}I_{rms}^{*}(h_1,f_i)\\I_{rms}^{*}(h_2,f_i)\\\cdots\\I_{rms}^{*}(h_k,f_i)\end{bmatrix}=\begin{bmatrix}S_{DFT}(I_{rms}(h_1))\\S_{DFT}(I_{rms}(h_2))\\\cdots\\S_{DFT}(I_{rms}(h_k))\end{bmatrix} \tag{14}$$

As can be seen from the datasheet [33] [34], the ESR is a non-linear curve that changes with frequency and temperature. In order to make the ESR(f_i) match with the $I_{rms}(f_i)$, the ESR(f_i) needs to be obtained when f_i varies from 20 Hz to 10 kHz. The ESR(f_i) is fitted by the neural network, as shown in Fig. 8. In the setting of the neural network, the input layers are the temperature and frequency, and the output layer is the ESR value. In the fitting results, the changes of the ESR are consistent with the datasheet. According to the training results of the neural network, after 200 iterations of learning, the error is less than 2%, which is highly acceptable.

Through the calculation, the profiles of I_{rms} and P_{loss} are represented in Fig. 9, where the oscillation degree of I_{rms} and P_{loss} have major changes at different working conditions. The extreme point of power loss also confirms the influence of the electrical stress profile.

B. Equivalent Thermal Modeling of the DC-Link Capacitor

The complex physical structure and dynamic power loss cause a large burden on the calculation of the physical modeling. To address this concern, a simplified mathematical model is used, instead of the physical model. In fact, the temperature cannot change suddenly and the temperature change is a gradual process. In order to accurately and quickly characterize the impact of electro-thermal tress, a thermal network model is established to estimate the hot spot temperature of capacitor banks.

According to the thermal model, when the power loss value is $P_{loss(1)}$ at t_1, the rise of the hot spot temperature ΔT_1 can be expressed as (the time interval is Δt) [35]:

This article has been accepted for publication in a future issue of this journal, but has not been fully edited. Content may change prior to final publication. Citation information: DOI 10.1109/JESTPE.2020.3000130, IEEE Journal of Emerging and Selected Topics in Power Electronics

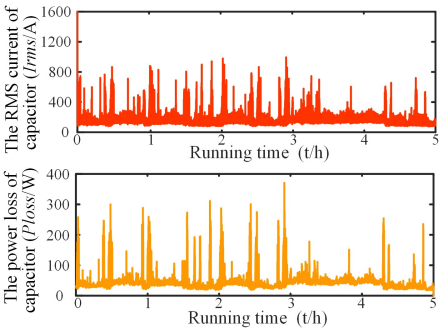

Fig. 9. Calculation results of the I_{rms} and P_{loss} of the DC-link capacitor.

$$\Delta T_1 = P_{loss(1)} \times \sum_{m=1}^{k} R_{th\_m} \left(1 - e^{\frac{\Delta t}{R_{th\_m} \times C_{th\_m}}} \right) \tag{15}$$

where R_{th_m} and C_{th_m} represent the thermal resistance and thermal capacity of the *m-th* layer in the equivalent thermal model, respectively. k is the total number of layers in the thermal network model.

Meanwhile, when the power loss value changes to $P_{loss(2)}$ at t_2, the rise of the hot spot temperature ΔT_2 can be expressed as:

$$\Delta T_2 = \Delta T_1 \times \sum_{m=1}^{k} e^{\frac{\Delta t}{R_{th\_m} \times C_{th\_m}}} + P_{loss(2)} \times \sum_{m=1}^{k} R_{th\_m} \left(1 - e^{\frac{\Delta t}{R_{th\_m} \times C_{th\_m}}} \right) \tag{16}$$

The rise of the hot spot temperature ΔT_n can be derived as

$$\Delta T_n = \sum_{i=1}^{n} \left[P_{loss(i)} \times \sum_{m=1}^{k} R_{th\_m} \left(e^{-\frac{(n-i)\Delta t}{R_{th\_m} \times C_{th\_m}}} - e^{-\frac{(n+1-i)\Delta t}{R_{th\_m} \times C_{th\_m}}} \right) \right] \tag{17}$$

Because of the cylindrical film and the hexagonal package, the physical structure of the DC-link capacitor banks has significant symmetry. Considering this, a bidirectional heat transfer is analyzed, which can be equivalent to the vertical direction and the horizontal direction, as shown in Fig. 10 [36].

The bidirectional equivalent thermal model of the capacitor banks is shown in Fig. 11. In the bidirectional thermal model, the heat is transferred in the horizontal and vertical directions, and the power losses in the horizontal and vertical directions are referred as $P_{loss\_x(i)}$ and $P_{loss\_y(i)}$, which satisfy the following relationship

$$\begin{cases} \Delta T_n = \sum_{i=1}^{n} \left[P_{loss\_U(i)} \times \sum_{m=1}^{k} R_{th\_Um} \left(e^{-\frac{(n-i)\Delta t}{R_{th\_Um} \times C_{th\_Um}}} - e^{-\frac{(n+1-i)\Delta t}{R_{th\_Um} \times C_{th\_Um}}} \right) \right] \\ P_{loss\_x(i)} + P_{loss\_y(i)} = P_{loss(i)} \end{cases} \tag{18}$$

where R_{th_Um} and C_{th_Um} (U=x,y) represent the thermal resistance and thermal capacity of the *m-th* layer in the horizontal direction or the vertical direction, respectively.

The thermal resistance R_{th_U1}~R_{th_U6} and heat capacity C_{th_U1}~C_{th_U6} in different layers can be calculated by referring to the results of the physical modeling. The thermal impedance Z_{th_Uj} of the *j-th* layer can be expressed as [37]

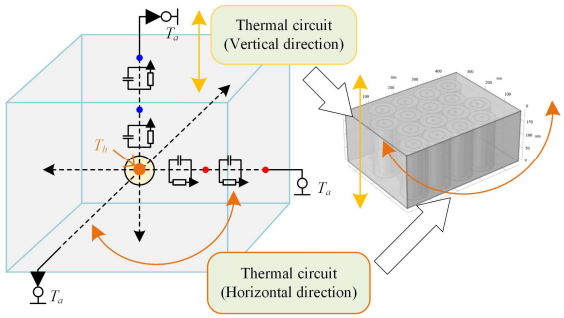

Fig. 10. Bidirectional heat transfer of the DC-link capacitor.

$$\begin{cases} Z_{th\_Uj} = \dfrac{T_{th\_Uj} - T_{th\_Uk}}{P_{loss\_U(i)}} \\ Z_{th\_Uj(t)} = R_{th\_Uj} \times \left(1 - e^{\frac{t}{R_{th\_Uj} \times C_{th\_Uj}}} \right) \end{cases} \tag{19}$$

where j and k represent the two adjacent layers. T_{th_Uj} and T_{th_Uk} represent the temperature values obtained by the physical modeling in the j and k layers, respectively.

According to the temperature changes of adjacent layers j and k at different time, the value of $Z_{th\_Uj(t)}$ can be obtained. Furthermore, $Z_{th\_Uj(t)}$ is fitted by the exponential function. Through the solution of parameter, the values of R_{th_U1}~R_{th_U6} and C_{th_U1}~C_{th_U6} in different layers are obtained [35].

Since the capacitor banks have multiple heat sources, the thermal coupling among the heat sources cannot be ignored. Inside the capacitor, there is a thermal coupling relationship between the one film core structure and the rest of the film core structures (the S. I between the layer.2 and the layer.3). In order to explore the relationship of thermal coupling, the film core p with the highest temperature is selected as the research object, and the remaining film core q is selected as the reference object. The thermal coupling can be regarded as the joint effect of the equivalent heat source and thermal resistance, which can be expressed as [26]

$$Z_{th\_x2\_pq} = \frac{T_{th\_x2(p)} - T_{th\_x2(q)}}{P_{loss\_x(i)}} \tag{20}$$

where Z_{x2_pq} is the equivalent thermal coupling impedance, $T_{th\_x2(p)}$ and $T_{th\_x2(q)}$ represent the temperature of the film cores p and q obtained in the multiple physical property modeling, respectively.

Similarly, outside the capacitor, the thermal coupling impedance Z_{y4_pq} (the S. II between the layer.4 and the layer.5) can be obtained.

It is worth noting that in the air layer inside the chassis, according to the influence of the gas convection, R_{th_U5} can be calculated as

$$R_{th\_U5} = \frac{1}{h_c A} \tag{21}$$

where h_c is the convection coefficient and A is the effective heat conduction area.

The effect of forced air-cooling heat dissipation depends on the shape of the object and the *Nusselt* number *Nu*. Based on

This article has been accepted for publication in a future issue of this journal, but has not been fully edited. Content may change prior to final publication. Citation information: DOI 10.1109/JESTPE.2020.3000130, IEEE Journal of Emerging and Selected Topics in Power Electronics

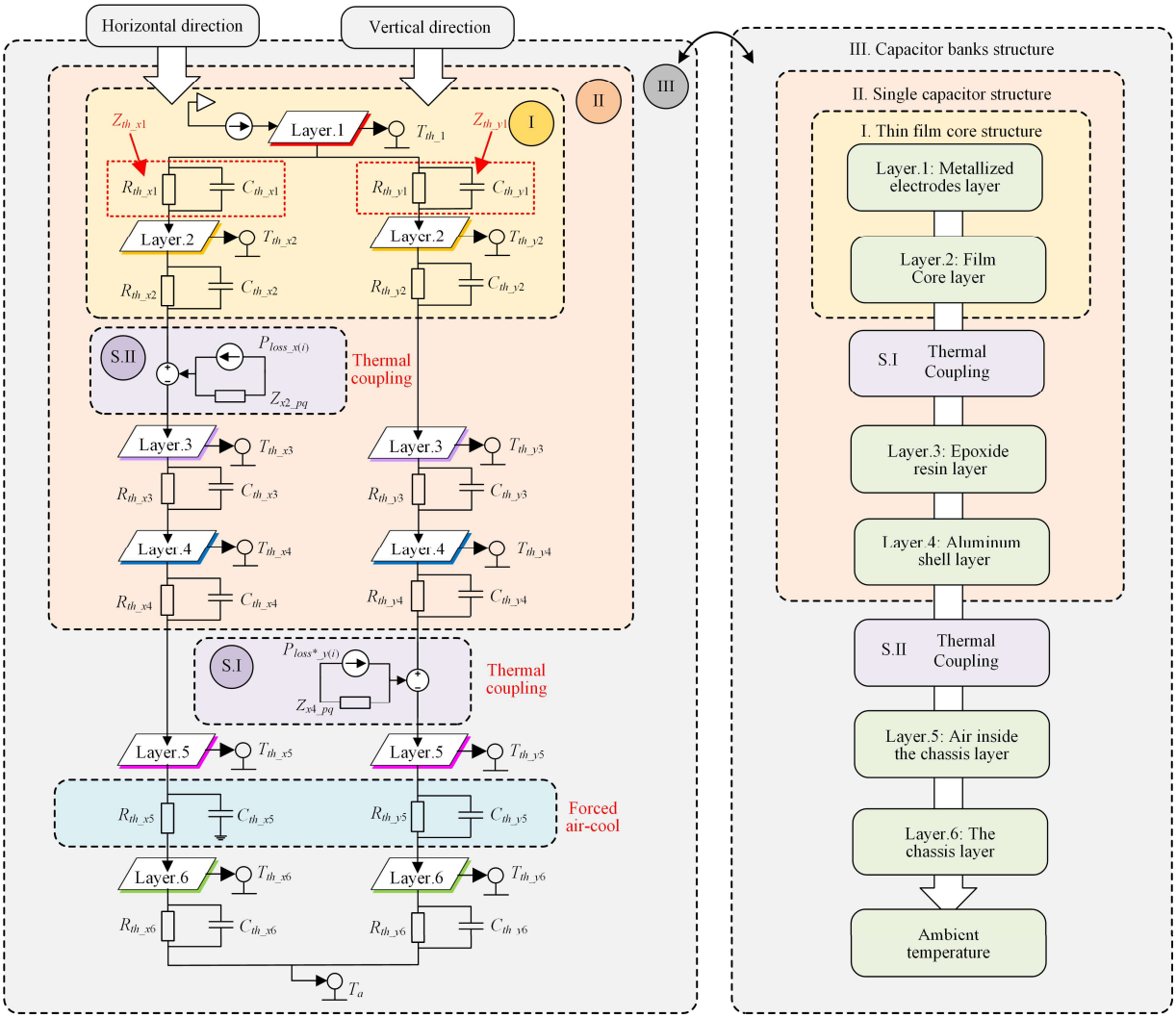

Fig. 11. Equivalent thermal model of the capacitor banks.

the summary of the flow patterns in [38] and [39], the Nusselt numbers of the capacitors in different positions are different. The *Nusselt* numbers of the No.1~2 capacitors and No.3~4 capacitors can be expressed as Nu_1 and Nu_2

$$h_{c1} = \frac{k}{l_c} Nu_1, h_{c2} = \frac{k}{l_c} Nu_2 \tag{22}$$

where k and l_c represent the thermal conductivity of dry air and the equivalent diameter, respectively.

Therefore, the thermal impedance of the No.1~2 capacitors and No.3~4 capacitors in the air layer needs to be considered separately, which can be respectively expressed as $Z_{th\_U5(No.1\sim2)}$ and $Z_{th\_U5(No.3\sim4)}$

$$\begin{cases} Z_{th\_U5(No.1\sim2)} = \dfrac{T_{th\_U6(No.1\sim2)} - T_{th\_U5(No.1\sim2)}}{P_{loss\_U(i)}} \\ Z_{th\_U5(No.3\sim4)} = \dfrac{T_{th\_U6(No.3\sim4)} - T_{th\_U5(No.3\sim4)}}{P_{loss\_U(i)}} \end{cases} \tag{23}$$

C. *Analysis results of electrothermal stress*

The overall flowchart of the thermal stress solution for the DC-link capacitor banks is shown in Fig. 12. Firstly, the physical model is given by setting the geometry, material, air cooling, and thermal element. Meanwhile, according to the bidirectional thermal model, the equivalent thermal model is established by calculating the parameters of the thermal resistance, thermal capacity and thermal coupling. Different positions of the physical model correspond to the layering of the equivalent thermal model, where the thermal parameters are verified by the actual temperature tests. And then, the power loss profile is substituted to calculate the hot spot temperature.

Fig. 13 shows the temperature calculation results for the hot spot temperature and the shell temperature layer in the equivalent thermal model, which shows the comparison of three situations in the equivalent thermal model:

I→ (the No.1~2 capacitors adding air cooling)
II→ (the No.3~4 capacitors adding air cooling)
III→ (no air cooling)

This article has been accepted for publication in a future issue of this journal, but has not been fully edited. Content may change prior to final publication. Citation information: DOI 10.1109/JESTPE.2020.3000130, IEEE Journal of Emerging and Selected Topics in Power Electronics

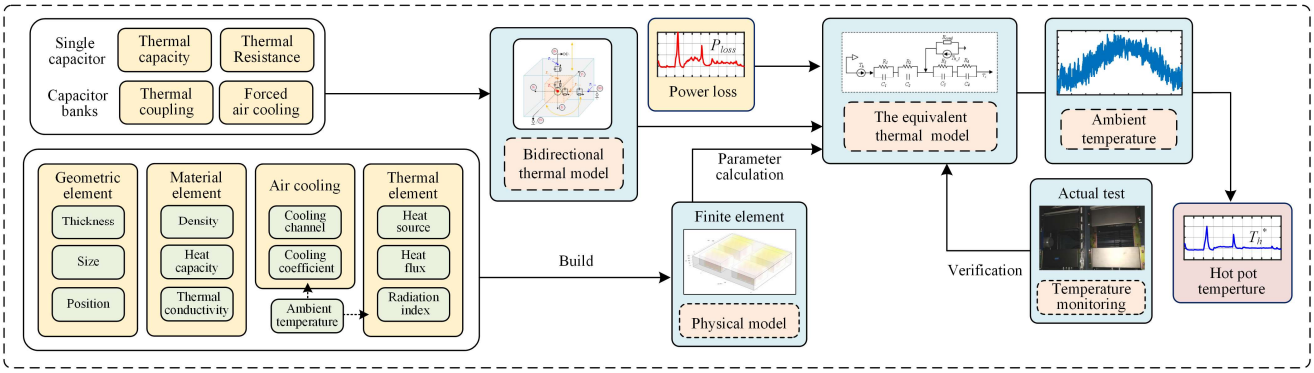

Fig. 12. Overall flowchart of thermal stress solution of the DC-link capacitor banks.

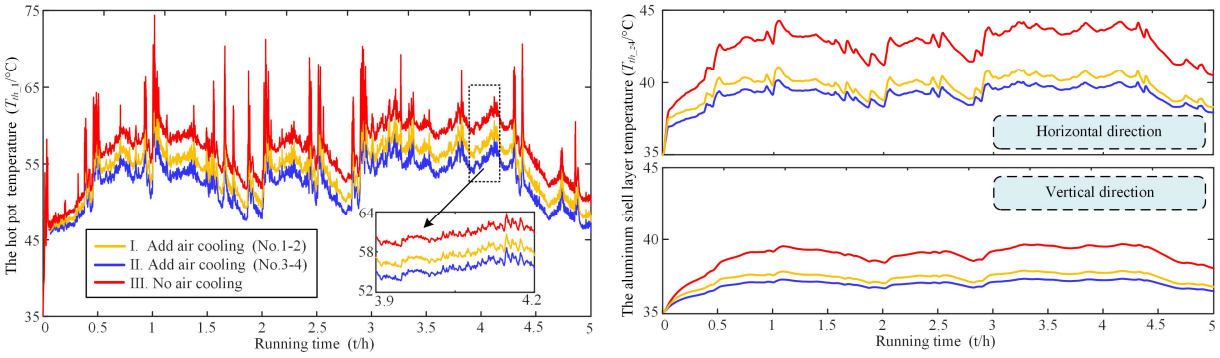

(a) (b)

Fig. 13. Temperature curve of thermal model simulation. (a) hot pot temperature. (b) case tempaerature.

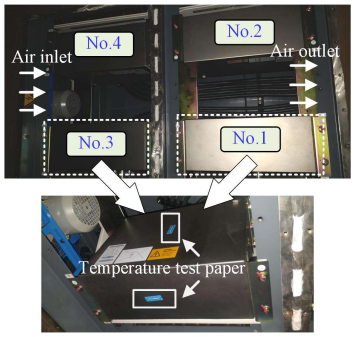

Fig. 14. Actual temperature test of DC-link capacitor in the railway traction drive system.

In the comparison of hot spot temperature, the temperature of the case III without the air-cooling is the highest. Considering the air-cooling heat dissipation, the temperature in the case II is slightly higher than that in the case I, which is in line with objective laws. Meanwhile, the change of the hot spot temperature in the equivalent thermal model is slower than the power loss, indicating that the heat capacity of the capacitor cannot be ignored. In the comparison of case temperature, the magnitude variation of the temperature in the horizontal direction is simultaneously larger than that in the vertical direction. According to the structure of the equivalent thermal model, the heat is emitted to the air through the metallized electrodes layer, the film core layer, the epoxide resin layer, and the aluminum shell layer. Since the thermal resistances are different in each layer, there is an obvious difference between the internal temperature and the external temperature of the capacitor.

The DC-link capacitor banks are located at the bottom of the train. Considering the safe operation of the system, it is difficult to directly install the temperature sensor for monitoring the temperature of the DC-link capacitor. To verify the accuracy of the equivalent thermal model, the highest case temperature of the DC-link capacitor is recorded through the temperature test papers. Considering the directions and positions of the capacitor banks, the temperature test papers are pasted in Fig. 14. After the train operation during one day, the temperature of the test papers are recorded, where the vertical temperature of the No. 1 and No. 3 capacitors do not exceed 40 °C, the horizontal temperature of the No. 3 capacitor is about 42 °C, and the horizontal temperature of the No. 1 capacitor is about 43 °C. According to the calculation of the equivalent thermal model (the highest ambient temperature in the test day is about 35.2 °C), the horizontal temperature of the No. 3 capacitor is about 41.1 °C, and the horizontal temperature of the No. 1 capacitor is about 42.4 °C. The test results are slightly higher than that of the equivalent thermal model. Considering the influence of other heat sources in the train body structure, the ambient temperature around the capacitor banks may be higher than that of external devices, so the result is reasonable.

This article has been accepted for publication in a future issue of this journal, but has not been fully edited. Content may change prior to final publication. Citation information: DOI 10.1109/JESTPE.2020.3000130, IEEE Journal of Emerging and Selected Topics in Power Electronics

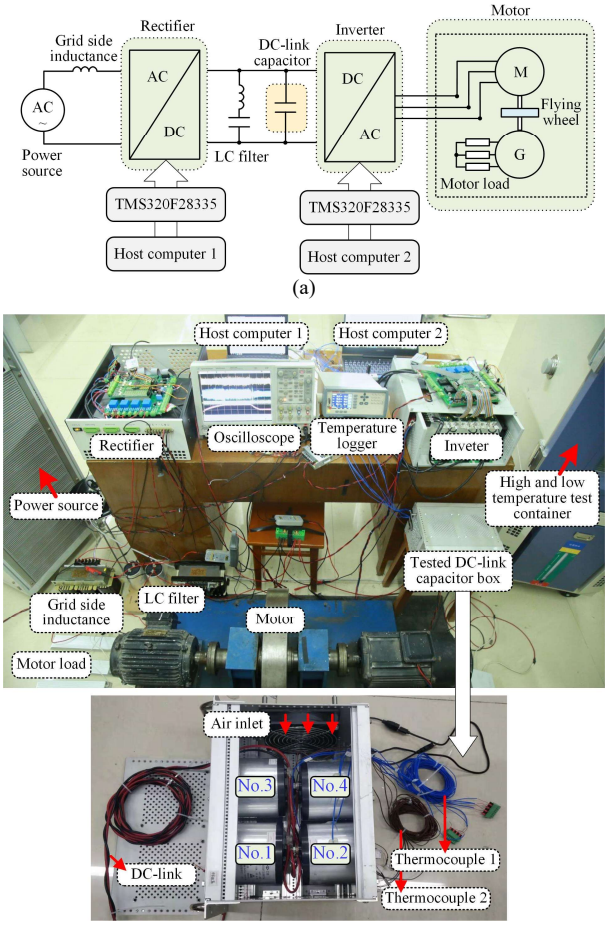

Fig. 15. Experimental test setup. (a) system structure. (b) test platform.

IV. Prototype Experiment of Electrical Stress and Thermal Stress

In order to verify the analysis rationality of the electrical and thermal stress analysis in the DC-link capacitor, the experimental prototype test is performed. The experimental prototype platform for the reliability test of the DC-link capacitor is shown in Fig. 15. Two TMS320F28335 digital signal processors are used as controllers for the rectifier and inverter, respectively. Meanwhile, the flywheel is used to increase the rotary inertia of the motor for simulating the railway operation. In addition, the parameters of the experimental prototype platform and the tested DC-link capacitors are given in the Appendix.

A. Electrical Stress Analysis

To investigate the impacts of multi-operation conditions on the electrical stress of the DC-link capacitor, the test cases under different running speed are performed. Fig. 16 shows the DC-link voltage U_{dc}, DC-link capacitor current I_{cap}, and running speed n_d under different motor speeds. The I, II, III, and IV represent the four operating stages of acceleration, uniform motion, braking, and stopping, respectively. Meanwhile, resistances are set to the range of 50 Ω to 150 Ω as load

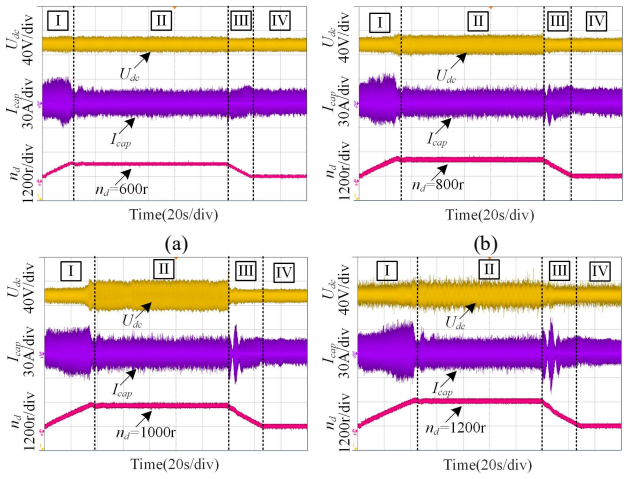

Fig. 16: Experimental results of the DC-link voltage U_{dc}, capacitor current I_{cap} and running speed n_d (Motor load = 150 Ω). (a) Speed = 600 r/min. (b) Speed = 800 r/min. (c) Speed = 1000 r/min. (d) Speed = 1200 r/min.

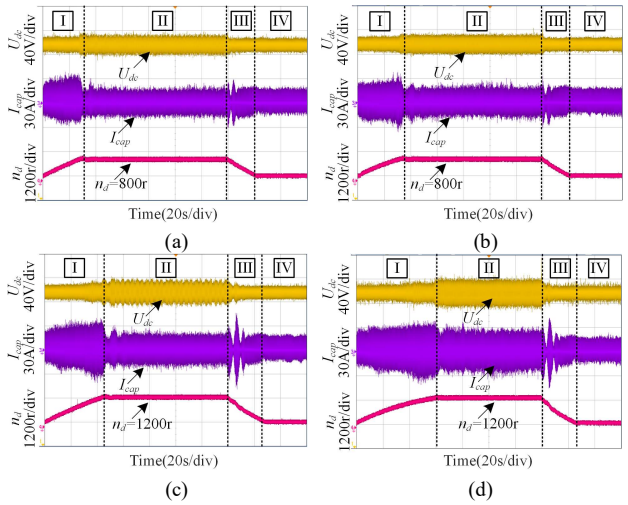

Fig. 17. Experimental results of the DC-link voltage U_{dc}, capacitor current I_{cap} and running speed n_d. (a) Speed = 800 r/min, Motor load = 100 Ω. (b) Speed = 800 r/min, Motor load = 50 Ω. (c) Speed = 1200 r/min, Motor load = 100 Ω. (d) Speed = 1200 r/min, Motor load = 50 Ω.

variations, simulating the influences of different slopes on the electrical stress of the DC-link capacitor. Fig. 17 shows the DC-link voltage U_{dc}, capacitor current I_{cap} and running speed n_d with different motor loads.

From the experimental results, it can be seen that the ripple of the DC-link capacitor current in the acceleration stage and the braking stage is larger than that in the uniform motion stage, while the ripples in the stop stage is the smallest. Moreover, under higher running speed and smaller motor load, the ripples of the capacitor current changes greatly.

In order to further quantify the effect of electrical stress, the THD value of the DC-link capacitor current are given in the Fig. 18, where the amplified waveform of the DC-link capacitor current is 20ms / div (select the output current I_N as the fundamental wave). It can be seen that the THD value of the DC link capacitor in the acceleration phase and the braking

This article has been accepted for publication in a future issue of this journal, but has not been fully edited. Content may change prior to final publication. Citation information: DOI 10.1109/JESTPE.2020.3000130, IEEE Journal of Emerging and Selected Topics in Power Electronics

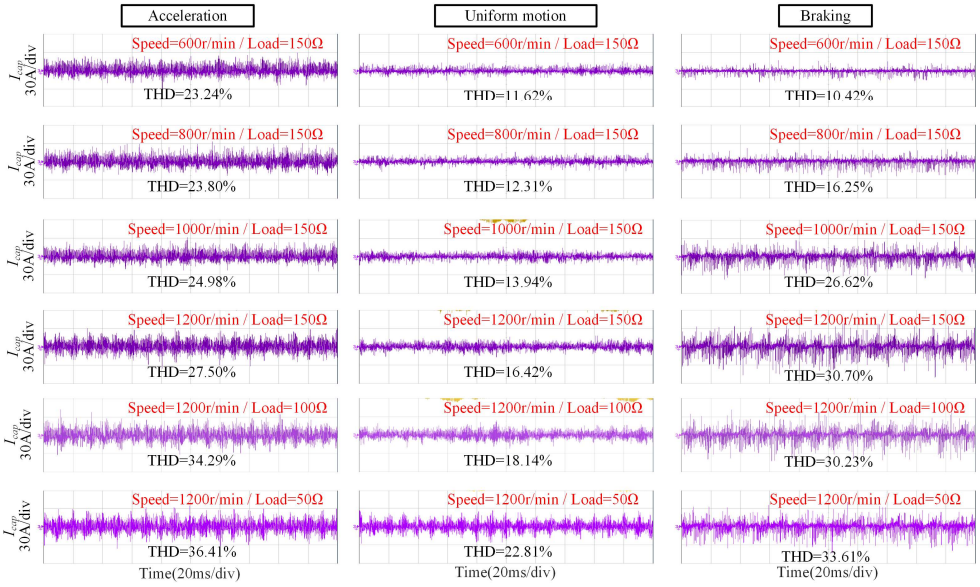

Fig. 18. Experimental amplified waveforms of DC-link capacitor current I_{cap} and the THD value.

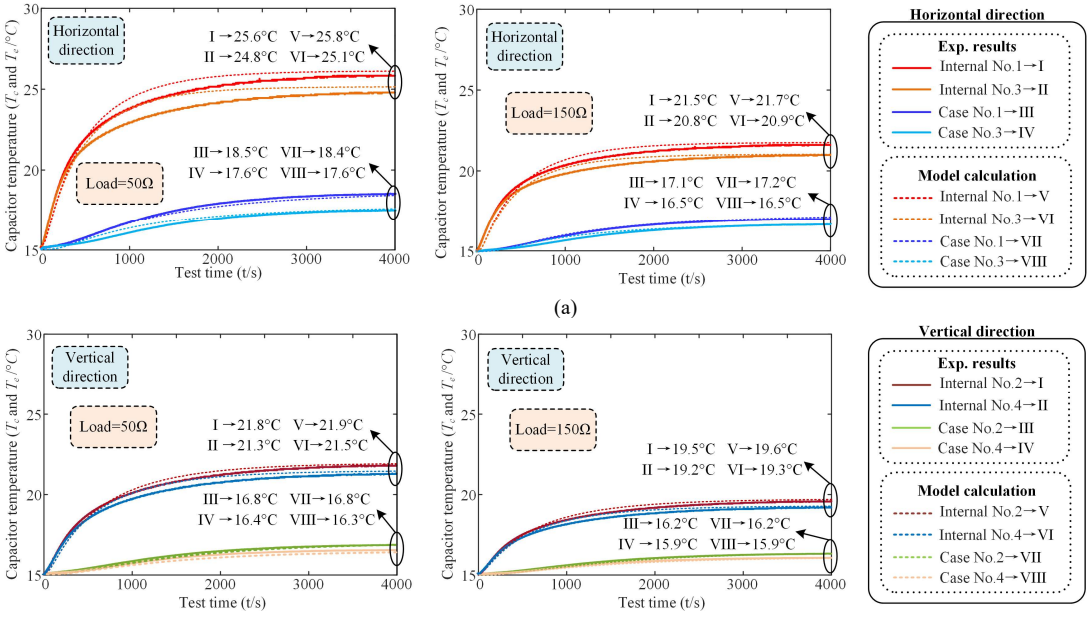

Fig. 19. Test temperature under different motor loads. (motor speed = 1200r/min). (a) horizontal direction. (b) vertical direction.

phase is about 1.5 to 2 times as much as the THD value in the uniform motion phase. With the increase of speed and motor load, the THD value gradually increases. The changing trend are consistent with that in the simulation model. The THD of I_{cap} in the experiment is slightly lower than the simulated THD, which may be due to the higher power level of the motor in the simulation model.

B. Thermal Stress Analysis

In order to verify the rationality of the thermal stress analysis, the test box is designed to place the DC-link capacitor banks. The thermocouples are buried in the epoxy layer inside the tested capacitors, and a fan is set to achieve forced air cooling, simulating the physical structure in the traction drive system, as shown in Fig. 15(b). The thermocouple 1 monitors the case temperature of the capacitor and the thermocouple 2 monitors the internal epoxy layer temperature of the capacitor. The thermocouples No.1 and No.3 are buried in the horizontal epoxy resin layer, whereas the thermocouples No.2 and No.4 are buried in the vertical epoxy resin layer. The temperature inside and outside the capacitor is monitored and recorded by a temperature logger. Fig. 19 shows the temperature rise

This article has been accepted for publication in a future issue of this journal, but has not been fully edited. Content may change prior to final publication. Citation information: DOI 10.1109/JESTPE.2020.3000130, IEEE Journal of Emerging and Selected Topics in Power Electronics

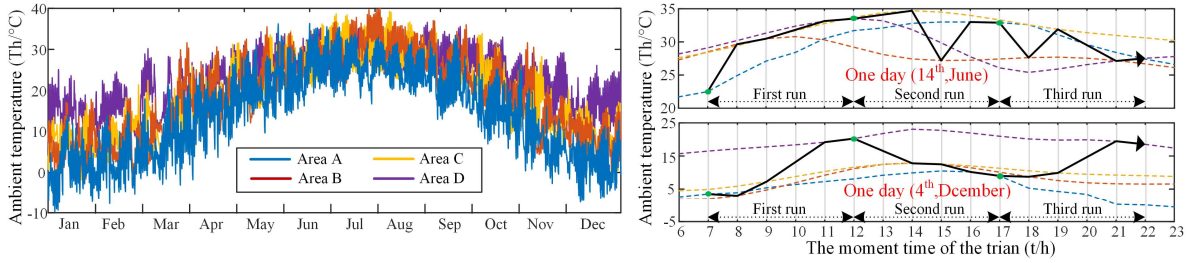

(a) (b)

Fig. 20. Mission profile waveform of ambient temperature. (a) in one year. (b) in one day.

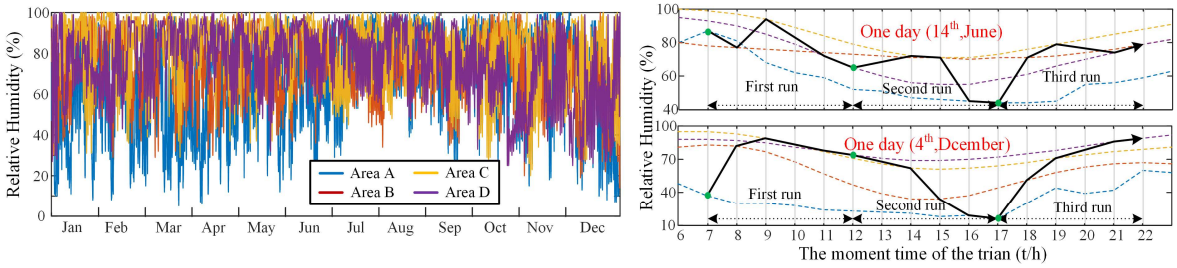

(a) (b)

Fig. 21. Mission profile waveform of relative humidity. (a) in one year. (b) in one day.

process of a capacitor with a load of 50 Ω and 150 Ω, respectively.

From the experimental results of thermal stress, it can be obtained that the change trend of the temperature rise is consistent with the harmonic analysis of the current in the electrical stress. That is shows the impact of different operation conditions on the electro-thermal stress of the capacitor cannot be ignored. Meanwhile, the rising temperature of the horizontal direction is higher than that of the vertical direction. Due to the forced air cooling, the rising temperature of No.1 ~ No.2 is slightly higher than that of No.3 ~ No.4. Furthermore, the data collected by the prototype experimental platform are substituted into the electro-thermal stress model, obtaining the rising temperature of the test capacitor under different operation conditions. The calculated results in the electro-thermal stress model are basically consistent with the change trend of the experimental data. The temperature rise error is less than 5%, which indicates the effectiveness of the electro-thermal analysis.

V. Lifetime Estimation of DC-Link Capacitor Banks

A. *DC-link Capacitor Lifetime Estimation*

Due to the long mileage of the actual running process of the train, it usually needs to passes through different latitude areas. The impact of the ambient temperature and the humidity cannot be ignored in the reliability analysis of capacitors. The ambient temperature and relative humidity of the four areas (A→B→C→D) that are mainly passed during the actual operation of the train are shown in Fig. 20(a) and Fig. 21(a). On the basis of the running time and distance of the four regions, the ambient temperature and relative humidity change within a single day are further obtained in Fig. 20(b) and Fig. 21(b). During the actual operation of the train, the mission profile from short-term operational timescales (one-day) to long-term operational timescales (one-year) is established under multi-regional operations.

According to the datasheet, the Failures in Time of capacitor is 100 (FIT=100), indicating that the damage rate reaching the rated lifetime (100000 h) of the sample is 1% [33].

For film capacitor, the lifetime model is given as [8] [40]

$$L=L_0\times\left(\frac{U_{dc}}{U_0}\right)^{-p}\times 2^{\frac{T_0-T_h}{10}}\times\left(\frac{RH}{RH_0}\right)^{-q} \tag{25}$$

where L and L_0 denote the actual lifetime and rated lifetime, U_{dc} and U_0 denote the actual capacitor voltage and rated capacitor voltage, RH and RH_0 represent actual relative humidity and rated relative humidity, T_0 and T_h denote the rated temperature and the hot spot temperature, and p and q represent two empirical coefficients, respectively.

Fig. 22 shows the detailed results of the expected lifetime distribution for the DC-link capacitors at different operating periods. In the one-day operation cycle, the lifetime expectancy distribution varies greatly with the change of the operation conditions, and the result is related to the dynamics variations of the electrical stress and the hot spot temperature. In terms of different dates, the lifetime expectancy distribution is directly related to the mission profiles of the ambient temperature and humidity. Furthermore, by using the *Miner* linear cumulative damage theory, the lifetime expectancy of the whole operation cycle can be obtained [41]. Finally, the expected lifetime $L_{(whole)}$ of the DC-link capacitor is about **50.64 years** (the damage rate is 1%).

B. *Accelerated Aging Experiments*

In order to verify the effectiveness of the lifetime expectancy, an accelerated aging experiment test is implemented. A higher ambient temperature T_a (increase 30°C) is set in high and low

This article has been accepted for publication in a future issue of this journal, but has not been fully edited. Content may change prior to final publication. Citation information: DOI 10.1109/JESTPE.2020.3000130, IEEE Journal of Emerging and Selected Topics in Power Electronics

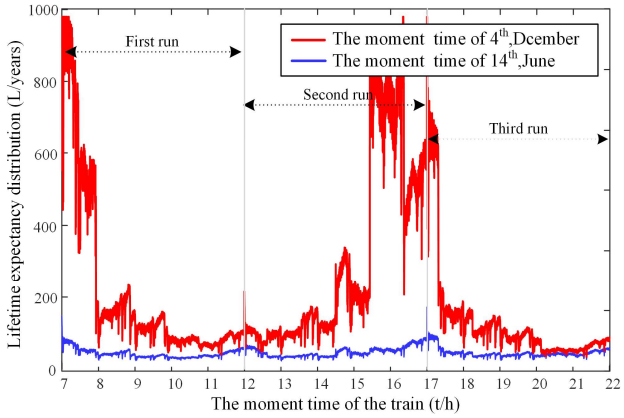

Fig. 22. Calculation results for the lifetime expectancy distribution.

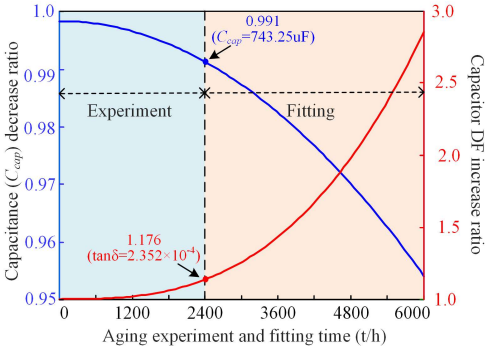

Fig. 23. Experimental and fitting results of the capacitance loss and DF increase.

temperature test container, and the DC-link voltage U_{dc} is increased to 1.2 times. For the increase of the ambient temperature and voltage, the acceleration factor $H_{(acc)}$ can be expressed as [42] [43] by using the *Generalized Eyring Relationship*.

$$H_{(acc)} = \left(\frac{U_{dc}}{1.2U_{dc}}\right)^{-p} \times 2^{\frac{(T_h+30)-T_h}{10}} \tag{26}$$

In this experiment, the acceleration factor $H_{(acc)}$ of the DC-link capacitor is set to 37.0. A typical end-of-life standard for film capacitor is that the C_{cap} reduces 5% and the dissipation factor (DF) increases to 3 times [8]. The DC-link capacitor is tested for about 2400 hours, and the value of C_{cap} and DF in the experiment are fitted as shown in Fig. 23. According to the failure criteria of the film capacitor, the experimental lifetime of the DC-link capacitor banks is about 6500 hours. After multiplied by the acceleration factor $H_{(acc)}$, the conversion lifetime of the DC-link capacitor is about 240500 hours (I.e., 43.93 years). Comparing the experimental results with the above lifetime expectancy, it is demonstrated that the results from the proposed models are available. Notice that the experimental results are slightly less than the expected lifetime expectancy. It might be resulted from the phenomenon that the influence of high temperature and high voltage on the capacitor is greater than the calculation result of the lifetime model.

C. *Electro-thermal Stress Effect of Capacitor Aging*

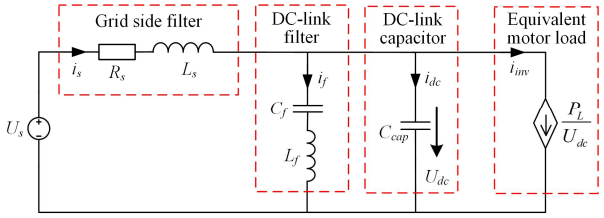

Fig. 24. Equivalent electrical model of the traction drive system

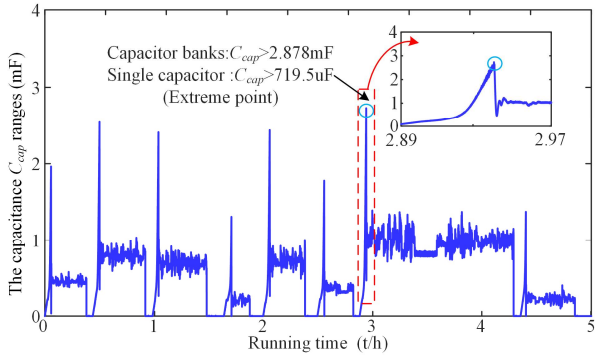

Fig. 25. Range of C_{cap} during the operation time based on the stability criteria.

a) *Capacitor Parameter Threshold According to Electrical Stress*

The equivalent electrical model of the traction drive system is shown in Fig. 24 [44]. The i_s, i_f, i_{dc} represent the grid side current, the LC filter current and the DC-link current, respectively. The converter and the motor load are equivalent to a controlled current source i_{inv}. The input power of the motor load is P_L. According to the stability criteria, the capacitance value C_{cap} should satisfy (27), as (More details see the Appendix A)

$$C_{cap} > \frac{33.76U_{dc}^4P_L - 93.75U_{dc}^2P_L^2}{0.762\times10^3U_{dc}^6 - 8.15\times10^3U_{dc}^4P_L - 9U_{dc}^2P_L^2} \tag{27}$$

According to the stability criterion, the range of C_{cap} depends on other electrical parameters and operating conditions in the traction drive system. When other electrical parameters maintain the constant values, the range of C_{cap} change in real time with the dynamic value of the DC-link voltage U_{dc} and the motor power P_L. Thus, the ranges of C_{cap} at different operation conditions are obtained in Fig. 25, which can be used for analyzing changes trend of C_{cap}. During the operating period, the maximum extreme point value of C_{cap} is approximately 719.5 μF in the single capacitor. When the C_{cap} is less than the extreme point, the system is electrically unstable, resulting in unsafe operation.

b) *Capacitor Parameter Threshold According to Thermal Stress*

With the capacitor aging, the long-term operation results in the increase of the DF, that is, the increase of the ESR. Furthermore, the increase in the ESR leads to the increase of the power loss. In the traction drive system, the maximum rated temperature of the film capacitor is 75°C. Accordingly,

This article has been accepted for publication in a future issue of this journal, but has not been fully edited. Content may change prior to final publication. Citation information: DOI 10.1109/JESTPE.2020.3000130, IEEE Journal of Emerging and Selected Topics in Power Electronics

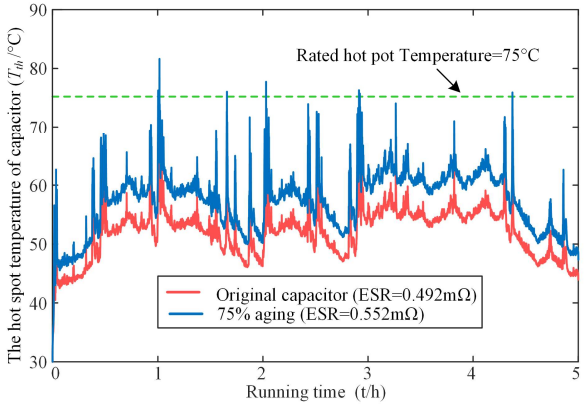

Fig. 26. Extreme point of the ESR based on the limit of rated temperature.

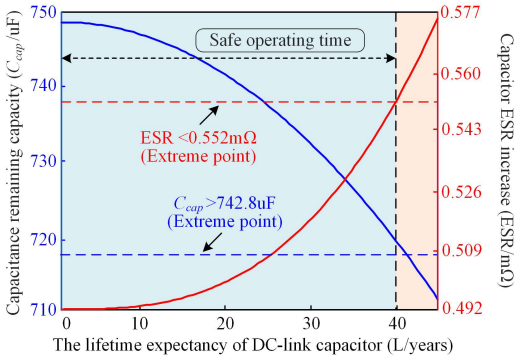

Fig. 27. Capacitance loss and ESR increase with an end-of-life standard adapted to the traction drive system.

the hot spot temperature must be kept as low as possible during the operation condition. The relationship of the DF and ESR can be expressed as [33]

$$ESR(f_i) = R_r + \frac{\tan\delta}{\omega \cdot C} \tag{28}$$

where R_r denotes the series resistance.

According to (28), with the capacitor aging, the ESR approximately increases from 0.492 mΩ to 0.577 mΩ. It can be seen that the hot spot temperature of the capacitor gradually increases with the aging of the capacitor, as shown in Fig. 26. When the temperature of the capacitor is higher than the rated temperature, the value of empirical coefficient p in the lifetime evaluation model continues to increase [33], causing the capacitor lifetime decays at a faster rate. When the capacitor operation at the extreme point (75% aging, ESR=0.552 mΩ), the hot spot temperature has exceeded the rated temperature for a large amount of time (there are 5 periods in a single operation cycle). When the ESR is higher than the extreme point, the system is thermally unstable, which is undesirable.

D. Reliability Evaluation of the DC-link Capacitors Banks

According to the safe operating requirement, the reduction of C_{cap} by 4.06% and the increase of the DF by 1.81 times are selected as the end-of-life standard adapting with the railway traction drive system. Comprehensively, the lifetime of unstable region prevails when the capacitance loss exceeds

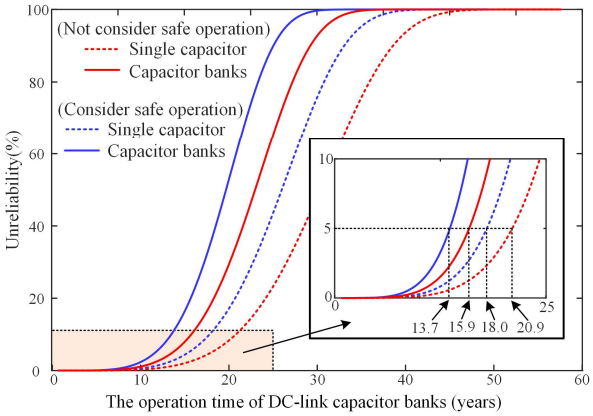

Fig. 28. Unreliability curve of single capacitor and capacitor banks.

75 %, as shown in Fig. 27. Finally, it can be concluded that the lifetime of the DC-link capacitor is approximately 39.75 years (the damage rate is 1%).

In order to further describe the detailed failure variation for the reliability of the capacitor banks, the unreliability of the capacitor banks is described by the Weibull distribution. The influence of the sample parameter variation and the uncertainty of the empirical coefficient on the failure time are considered

$$F(x) = 1 - e^{-(\frac{x}{\eta})^m} \tag{29}$$

It is assumed that the Weibull shape parameters are invariant in the same failure mode [17]. The variation of the loss rate in the aging experiment is fitted to determine the shape parameter of the Weibull distribution m= 5.06. With and without considering the safe operation, the proportional parameters η are 201240 and 234780, respectively. Based on the results of the lifetime evaluation, the unreliability distribution of DC-link capacitor can be obtained. As shown in Fig. 28, considering the relevant standards [45], when the unreliability rate reaches 5% (the damage rate is 0.05%), the operation time of the single capacitor and capacitor banks without the consideration of safe operation are 20.9 years and 15.9 years, respectively. However, the operation time of single capacitor and capacitor banks with the consideration of safe operation are 18.0 years and 13.7 years under the 5% unreliability rate, respectively.

V. Conclusions

In this paper, a reliability evaluation method of the DC-link capacitor banks is proposed for the railway traction drive system. According to the analysis of electrical stress, thermal stress, electro-thermal stress coupling and end-of-life standard, the lifetime bottleneck of the capacitor banks can be reasonably solved. The analysis results can provide a reference to use the lower-cost on-condition maintenance (OCM), instead of the scheduled maintenance in the railway system. A case study has been conducted, and it can be concluded that:

1) For the electro-thermal coupling, the dynamic profile of the capacitor power loss is obtained by the sliding-window DFT and the neural network, which is consistent with the change of the RMS current.

This article has been accepted for publication in a future issue of this journal, but has not been fully edited. Content may change prior to final publication. Citation information: DOI 10.1109/JESTPE.2020.3000130, IEEE Journal of Emerging and Selected Topics in Power Electronics

2) The bidirectional thermal model shows that the influence of the heat capacity, the thermal coupling and the air-cooling heat dissipation in the capacitor banks cannot be ignored. Meanwhile, there are some obvious differences in the horizontal and vertical heat transfer of the capacitor.

3) Through the analysis of stability and the rated temperature limitation, an end-of-life standard satisfying the safe operation in the railway traction drive system can be obtained. Consequently, a more reasonable lifetime evaluation results of the DC-link capacitor banks present the Weibull distribution.

APPENDIX A
STABILITY ANALYSIS OF THE TRACTION DRIVE SYSTEM

The DC link equation is constructed and the small signal model at a static working point can be described as [44]

$$\begin{cases} U_s+\Delta u_s = R_s(I_s+\Delta i_s)+L_s\dfrac{d(I_s+\Delta i_s)}{dt}+U_{dc}+\Delta u_{dc} \\ U_{dc}+\Delta u_{dc} = \dfrac{1}{C_{cap}}\int (I_{dc}+\Delta i_{dc})dt \\ U_{dc}+\Delta u_{dc} = L_f\dfrac{d(I_f+\Delta i_f)}{dt}+\dfrac{1}{C_f}\int (I_f+\Delta i_f)dt \\ I_s+\Delta i_s = I_{dc}+\Delta i_{dc}+I_f+\Delta i_f+i_{inv} \end{cases} \tag{A.1}$$

Using the Taylor expansion of the expression and ignoring its quadratic term, the output current i_{inv} can be expressed as

$$i_{inv}=\frac{P_L}{u_{dc}}=\frac{P_L}{U_{dc}+\Delta u_{dc}}=\frac{P_L}{U_{dc}}\frac{1}{1+\Delta u_{dc}/U_{dc}}\approx\frac{P_L}{U_{dc}}-\frac{P_L\Delta u_{dc}}{U_{dc}^{\ 2}} \tag{A.2}$$

Substituting (A.2) into equation (A.1) and performing Laplace transform yield (A.1)

$$\begin{cases} \Delta u_s = R_s\Delta i_s+L_s\Delta i_s s+\Delta u_{dc} \\ \Delta u_{dc} = \dfrac{1}{C_{cap}}\Delta i_{dc}\dfrac{1}{s} \\ \Delta u_{dc} = L_f\Delta i_f s+\dfrac{1}{C_f}\Delta i_f\dfrac{1}{s} \\ I_s+\Delta i_s = \Delta i_{dc}+\Delta i_f-\dfrac{P_L}{U_{dc}^{\ 2}}\Delta u_{dc} \end{cases} \tag{A.3}$$

The closed-loop transfer function of the system can be obtained as

$$\begin{cases} \dfrac{\Delta u_{dc}}{\Delta u_s} = \dfrac{\left[U_{dc}^2L_fC_f\right]s^2+U_{dc}^2}{\left[\lambda_4\right]s^4+\left[\lambda_3\right]s^3+\left[\lambda_2\right]s^2+\left[\lambda_1\right]s+\left[\lambda_0\right]} \\ \lambda_4 = U_{dc}^2C_{cap}L_fL_sC_f \\ \lambda_3 = U_{dc}^2C_{cap}L_fC_fR_s-P_LL_sL_fC_f \\ \lambda_2 = U_{dc}^2L_sC_f+U_{dc}^2C_{cap}L_s+U_{dc}^2L_fC_f-P_LR_sL_fC_f \\ \lambda_1 = U_{dc}^2C_fR_s+U_{dc}^2R_sC_{cap}-L_sP_L \\ \lambda_0 = U_{dc}^2-P_LR_{sL} \end{cases} \tag{A.4}$$

To ensure that the system is progressively stable, the following equations should be satisfied

$$\begin{cases} \lambda_4>0,\ \ \lambda_3>0,\ \ \lambda_0>0, \\ b_1=\dfrac{\lambda_2\lambda_3-\lambda_1\lambda_4}{\lambda_3}>0 \\ c_1=\dfrac{\lambda_1b_1-\lambda_3\lambda_1}{b1}>0 \end{cases} \tag{A.5}$$

Substituting the parameters of the equivalent circuit and other circuit parameters, the equation (26) can be obtained.

APPENDIX B

TABLE B.I
EQUIVALENT THERMAL PARAMETERS OF THE CAPACITOR BANKS

Horizonal direction						
Thermal Resistance (K/W)	R_{th_1}	R_{th_x2}	R_{th_x3}	R_{th_x4}	R_{th_x5}	R_{th_x6}
Value	0.126	0.24	0.39	0.028	0.048	0.0028
Thermal Capacitance (J/W)	C_{th_1}	C_{th_x2}	C_{th_x3}	C_{th_x4}	C_{th_x5}	C_{th_x6}
Value	3.4	12.5	720	587	152	15.2
Vertical direction						
Thermal Resistance (K/W)	R_{th_1}	R_{th_z2}	R_{th_z3}	R_{th_z4}	R_{th_z5}	R_{th_z6}
Value	0.426	0.74	0.53	0.071	0.152	0.0072
Thermal Capacitance (J/W)	C_{th_1}	C_{th_z2}	C_{th_z3}	C_{th_z4}	C_{th_z5}	C_{th_z6}
Value	3.4	50.9	1600	412	287	9.1

TABLE. B.II
EXPERIMENTAL PLATFORM AND TESTED CAPACITOR PARAMETERS

	Experimental platform
Grid side voltage/frequency	380V / 50Hz
Grid side inductance	6.0 mH
Switching frequency	900Hz (rectifier) / 1000Hz (inverter)
DC-Link voltage	500V
Filter inductor/capacitor	L_f=3mH / C_f=0.84mF
Motor rated power/ frequency	3.3 kV•A / 50Hz
Prototype DC-link capacitor parameters (Four parallel)	
Capacitance C_{cap}	2mF (0.5mF×4)
Rated voltage V_{cap}	600V
ESR (1KHz/20°C)	3.0mΩ
Thermal resistance R_{th}	5.6K/W
Rate load lifetime	100000h (70°C)
Dielectric dissipation factor	$\tan\delta_0=2\times10^{-4}$
The range of hot pot temperature	-50~75°C

REFERENCES

[1] F. Schmid and C. J. Goodman, "Overview of electric railway systems," in *IET 13th Professional Develop. Course on Electric Traction Syst.*, London, 2014, pp. 1-15.

[2] S. Huang and M. Wu, "Reliability evaluation system for traction power supply system of electric railways," in *2018 IEEE 9th Int. Conf. on Software Eng. and Service Sci. (ICSESS)*, Beijing, China, 2018, pp. 441-444.

[3] S. Guo, Z. Rong, J. Yao, and H. Wang, "Reliability modeling and assigning method for HXD electric locomotive," in *2013 Int. Conf. on Qual., Rel., Risk, Maintenance, and Saf. Eng. (QR2MSE)*, Chengdu, 2013, pp. 289-295.

[4] D. Feng, S. Lin, Q. Yang, X. Lin, Z. He, and W. Li, "Reliability evaluation for traction power supply system of high-speed railway considering relay protection," *IEEE Trans. Transport. Electrific.*, vol. 5, no. 1, pp. 285-298, Mar. 2019.

[5] S. K. Chen, T. K. Ho, and B. H. Mao, "Reliability evaluations of railway power supplies by fault-tree analysis," *IET Electric Power Appl.*, vol. 1, no. 2, pp. 161-172, Mar. 2007.

[6] B. Yao, X. Ge , L. Shu, H. Wang, Z. Hu, and B. Gou. "Life estimation of DC-link capacitor in multi-operating traction drive system," in *2019 IEEE 10th Int. Conf. on Power Electron. (ICPE-ECCE Asia)*, Busan, 2019, pp. 2743-2748.

[7] H. Wang, M. Liserre, and F. Blaabjerg, "Toward reliable power electronics: Challenges, design tools, and opportunities," *IEEE Ind. Electron. Mag.*, vol. 7, no. 2, pp. 17-26, Jun. 2013.

[8] H. Wang and F. Blaabjerg, "Reliability of capacitors for DC-link applications in power electronic converters−an overview," *IEEE Trans. Ind. Appl.*, vol. 50, no. 5, pp. 3569-3578, Sep./Oct. 2014.

[9] B. Sun, X. Fan, C. Qian, and G. Zhang, "Pof-simulation-assisted reliability prediction for electrolytic capacitor in led drivers," *IEEE Trans. Ind. Electron.*, vol. 63, no. 11, pp. 6726-6735, Nov. 2016.

[10] K. Urata and T. Shimizu, "Temperature estimation of aluminum electrolytic capacitor under actual circuit operation," in *2018 Int. Power Electron. Conf. (IPEC-Niigata 2018 -ECCE Asia)*, Niigata, 2018, pp. 302-308.

[11] H. Wang, P. Davari, H. Wang, D. Kumar, F. Zare, and F. Blaabjerg, "Lifetime estimation of DC-link capacitors in adjustable speed drives under grid voltage unbalances," *IEEE Trans. Power Electron.*, vol. 34, no. 5, pp. 4064-4078, May 2019.

[12] H. Wen, W. Xiao, X. Wen, and P. Armstrong, "Analysis and evaluation of DC-link capacitors for high-power-density electric vehicle drive systems," *IEEE Trans. Veh. Technol.*, vol. 61, no. 7, pp. 2950-2964, Sep., 2012.

[13] M. Horák and P. Mach, "Study of thermal ageing of polypropylene film capacitors," in *2015 IEEE 21st Int. Symp. for Des. and Technol. in Electron. Packag. (SIITME)*, Brasov, 2015, pp. 57-60.

[14] Z. Li *et al*., "Lifetime prediction of metallized film capacitors based on capacitance loss," *IEEE Trans. Plasma Sci.*, vol. 41, no. 5, pp. 1313-1318, May 2013.

[15] K. Ma, H. Wang, and F. Blaabjerg, "New Approaches to Reliability Assessment: Using physics-of-failure for prediction and design in power electronics systems," *IEEE Power Electron. Mag.*, vol. 3, no. 4, pp. 28-41, Dec. 2016.

[16] D. Zhou, H. Wang, and F. Blaabjerg, "Mission profile based system-level reliability analysis of DC/DC converters for a backup power application," *IEEE Trans. Power Electron.*, vol. 33, no. 9, pp. 8030-8039, Sep. 2018.

[17] D. Zhou, Y. Song, Y. Liu, and F. Blaabjerg, "Mission profile based reliability evaluation of capacitor banks in wind power converters," *IEEE Trans. Power Electron.*, vol. 34, no. 5, pp. 4665-4677, May 2019.

[18] Y. Yang, A. Sangwongwanich, and F. Blaabjerg, "Design for reliability of power electronics for grid-connected photovoltaic systems," *CPSS Trans. Power Electron. Appl.*, vol. 1, no. 1, pp. 92-103, Dec. 2016.

[19] A. Sangwongwanich, Y. Yang, D. Sera, F. Blaabjerg, and D. Zhou, "On the impacts of PV array sizing on the inverter reliability and lifetime," *IEEE Trans. Ind. Appl.*, vol. 54, no. 4, pp. 3656-3667, Jul./Aug. 2018.

[20] A. Sangwongwanich, Y. Yang, D. Sera, and F. Blaabjerg, "Mission profile-oriented control for reliability and lifetime of photovoltaic inverters," *IEEE Trans. Ind. Appl.*, vol. 56, no. 1, pp. 601-610, Jan./Feb. 2020.

[21] M. Wang, B. Kou, and X. Zhao, "Analysis of energy consumption characteristics based on simulation and traction calculation model for the CRH electric motor train units," in *2018 21st Int. Conf. on Elect. Mach. and Syst. (ICEMS)*, Jeju, 2018, pp. 2738-2743.

[22] B. Yao, X. Ge, H. Wang, H. Wang, D. Zhou, and B. Gou, "Multitimescale Reliability Evaluation of DC-Link Capacitor Banks in Metro Traction Drive System," *IEEE Trans. Transport. Electrific.*, vol. 6, no. 1, pp. 213-227, Mar. 2020.

[23] Z. Li *et al*., "Temperature rise of metallized film capacitors in repetitive pulse applications," *IEEE Trans. Plasma Sci.*, vol. 43, no. 6, pp. 2038-2045, Jun. 2015.

[24] L. Wei, M. Wu, M. Yan, S. Liu, Q. Cao, and H. Wang, "A Review on Electrothermal Modeling of Supercapacitors for Energy Storage Applications," *IEEE J. Emerg. Sel. Topics Power Electron.*, vol. 7, no. 3, pp. 1677-1690, Sep. 2019.

[25] H. Wang, and H. Wang, "An analytical circuit based nonlinear thermal model for capacitor banks," *Microelectron. Rel.*, vol. 88, pp. 524-527, Jun. 2018.

[26] H. Wang, Q. Wang, and H. Wang, "A Lumped Thermal Model Including Thermal Coupling Effects and Boundary Conditions for Capacitor Banks," in *2018 Int. Power Electron. Conf. (IPEC-Niigata 2018 -ECCE Asia)*, Niigata, 2018, pp. 2421-2425.

[27] B. Gou, X. Ge, S. Wang, X. Feng, J. B. Kuo, and T. G. Habetler, "An open-switch fault diagnosis method for single-phase PWM rectifier using a model-based approach in high-speed railway electrical traction drive system," *IEEE Trans. Power Electron.*, vol. 31, no. 5, pp. 3816-3826, May 2016.

[28] B. Yao, D. Xie, Y. Zhang, X. Ge, and B. Gou, "The optimized lifetime model of DC-link capacitor considering power module faults in traction drive system," in *2019 22nd Int. Conf. on Elect. Mach. and Syst. (ICEMS)*, Harbin, China, 2019, pp. 1-4.

[29] X. Jiang, H. Hu, X. Yang, Z. He, Q. Qian, and P. Tricoli, "Analysis and adaptive mitigation scheme of low-frequency oscillations in AC railway traction power systems," *IEEE Trans. Transport. Electrific.*, vol. 5, no. 3, pp. 715-726, Sep. 2019.

[30] B. K. Bose, *Power Electronics and AC Drives*. Englewood Cliffs, NJ: Prentice-Hall, 1986.

[31] J. W. Kolar and S. D. Round, "Analytical calculation of the RMS current stress on the DC-link capacitor of voltage-PWM converter systems," *IEE Proc. - Electric Power Appl.*, vol. 153, no. 4, pp. 535-543, Jul. 2006.

[32] K. Laadjal, M. Sahraoui, A. J. M. Cardoso, and A. M. R. Amaral, "Online estimation of aluminum electrolytic-capacitor parameters using a modified Prony's method," *IEEE Trans. Ind. Appl.*, vol. 54, no. 5, pp. 4764-4774, Sep./Oct. 2018.

[33] Capacitors for power electronics, Electronicon, Germany, 2018. [Online]. Available: http://www.powercapacitors.info/download/200. 003-020021_App-notes.pdf

[34] Type polypropylene, DC link capacitors, CDE, Amercian, 2016. [Online]. Available: https://www.cde.com/resources/catalogs/947D.pdf

[35] A. S. Bahman, K. Ma, P. Ghimire, F. Iannuzzo and F. Blaabjerg, "A 3-D-lumped thermal network model for long-term load profiles analysis in high-power IGBT modules," *IEEE J. Emerg. Sel. Topics Power Electron.*, vol. 4, no. 3, pp. 1050-1063, Sept. 2016.

[36] W. Sarwar, M. Marinescu, N. Green, N. Taylor, and G. Offer, "Electrochemical double layer capacitor electro-thermal modelling," *J. Energy Storage*, vol. 5, pp. 10–24, Feb. 2016.

[37] A. Hijazi, P. Kreczanik, E. Bideaux, P. Venet, G. Clerc, and M. Di Loreto, "Thermal network model of supercapacitors stack," *IEEE Trans. Ind. Electron.*, vol. 59, no. 2, pp. 979-987, Feb. 2012.

[38] E. M. Sparrow, J. P. Abraham, and J. C. K. Tong, "Archival correlations for average heat transfer coefficients for non-circular and circular cylinders and for spheres in cross-flow," *International Journal of Heat and Mass Transfer*, vol. 47, pp. 5286–5287, Jun. 2004.

[39] W. A. Khan, J. R. Culham, and M. M. Yovanovich, "Convection heat transfer from tube banks in crossflow: analytical approach," *International Journal of Heat and Mass Transfer*, vol. 49, pp. 4832–4838, Aug. 2006.

[40] H. Wang, P. Diaz Reigosa, and F. Blaabjerg, "A humidity-dependent lifetime derating factor for DC film capacitors," *2015 IEEE Energy Convers. Congr. and Expo. (ECCE)*, Montreal, QC, 2015, pp. 3064-3068.

[41] Todinov M T. "Necessary and sufficient condition for additivity in the sense of the Palmgren–Miner rule," *Comput. Mater. Sci.*, 2001, 21(1): 101-110.

[42] BS EN 61881-1:2011:Raliway applications-rolling stock equipement-capacitors for power electronics

[43] E. Redondo-Iglesias, P. Venet, and S. Pelissier, "Global model for self-discharge and capacity fade in lithium-ion batteries based on the generalized eyring relationship," *IEEE Trans. Veh. Technol.*, vol. 67, no. 1, pp. 104-113, Jan. 2018.

[44] H. Wang, X. Ge, and Y. Liu, "An active damping stabilization scheme for the suppression of the DC-link oscillation in metro traction drive system," *IEEE Trans. Ind. Appl.*, vol. 54, no. 5, pp. 5113-5123, Sep./Oct. 2018.

[45] GB/T Standard Voltages, GB/T 21562.2, 2015. Railway applications-Specification and demonstration of reliability, availability, maintainability and safety (RAMS)-Rart 2: Guide to the application for safety.

This article has been accepted for publication in a future issue of this journal, but has not been fully edited. Content may change prior to final publication. Citation information: DOI 10.1109/JESTPE.2020.3000130, IEEE Journal of Emerging and Selected Topics in Power Electronics

Bo Yao (S'17) received the B.Eng. degrees in electrical engineering from Southwest Jiaotong University (SWJTU), Chengdu, China, in 2017. He is currently working toward the M.Eng. degree in electrical engineering at the Southwest Jiaotong University, Chengdu, China.

His research interest is the reliability-oriented lifetime evaluation, design optimization, and condition monitoring of power electronic devices.

Mr. Yao was a recipient of the Best Paper Award of International Conference on Electrical Machines and Systems (ICEMS) in 2019.

Xinglai Ge (M'15) received the B.S., M.S., and Ph.D. degrees in electrical engineering from Southwest Jiaotong University (SWJTU), Chengdu, China, in 2001, 2004, and 2010, respectively. He is currently a Full Professor in the School of Electrical Engineering, Southwest Jiaotong University and a Vice Director of Department of Power Electronics and Power Drive.

From July to August of 2012, he was a visiting scholar at George Mason University, VA, USA. From October 2013 to October 2014, he was a visiting scholar at the School of Electrical and Computer Engineering, Georgia Institute of Technology, Atlanta, GA, USA. He is the author and co-author of more than 60 technical papers

His research interests include stability analysis and control of electrical traction system, fault diagnosis and hardware-in-the-loop simulation of traction converter and motor drive system.

Dong Xie (S'17) was born in Sichuan, China, in 1995. He received the B.S. degree in electrical engineering from Southwest Jiaotong University, Chengdu, China, in 2017. He is currently working toward the Ph.D. degree in electrical engineering with the School of Electrical Engineering, Southwest Jiaotong University, Chengdu, China.

His research interests include fault diagnosis and fault-tolerant control of power electronic traction transformers for the traction system.

Songtao Li received the B.Sc. degree in electrical engineering from the Lanzhou University of Technology, Lanzhou, China, in 2018. He is currently pursuing the M.Sc. degree in power electronics and electrical drives with the School of Electrical Engineering, Southwest Jiaotong University, Chengdu, China.

His current research interests include permanent magnet synchronous motor drives and position sensorless control.

Yichi Zhang received the B.Eng. degrees in electrical engineering from Shenyang Agricultural University, Shenyang, China, in 2017. He is currently working toward the M.Eng. degree in electrical engineering at the Southwest Jiaotong University, Chengdu, China.

His research interests include the reliability and condition monitoring of power electronic system.

Huimin Wang (S'17) received the B.Eng. degrees in electrical engineering from Southwest Jiaotong University (SWJTU), Chengdu, China, in 2016. He is currently working toward the Ph.D. degree in electrical engineering at the Southwest Jiaotong University, Chengdu, China.

His research interests include linear induction motor drive system and its speed-sensorless control.

Mr. Wang was a recipient of the Best Paper Award of IEEE Transportation Electrification Conference and EXPO Asia-Pacific (ITEC Asia-Pacific) in 2019.

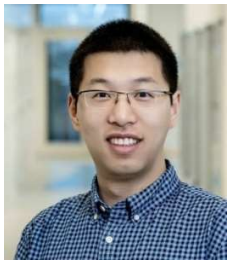

Haoran Wang (S'15-M'18) received the B.S. and M.S. degrees in control science and engineering from Wuhan University of Technology, Wuhan, China, in 2012 and 2015, respectively, and the Ph.D. degree in power electronics from Center of Reliable Power Electronics (CORPE), Aalborg University, Aalborg, Denmark, in 2018, where he is currently an Assistant Professor. From Jul. 2013 to Sep. 2014, he was research assistant with the Department of Electrical Engineering, Tsinghua University, Beijing, China. He was a Visiting Scientist with the ETH Zurich, Switzerland, from Dec. 2017 to Apr. 2018.

His research interests include capacitors in power electronics, reliability of power electronic systems, and multi-objective life-cycle performance optimization of power electronic systems.